Journal of Coupled Systems and Multiscale Dynamics

doi:10.1166/jcsmd.2014.1052
J. Coupled Syst. Multiscale Dyn.
Vol. 2(3)/2330-152X/2014/169/009

Spray drag effect of fluidized sand for a supersonic vehicle

Lakhdar Remaki[1,2,*], Oubay Hassan[2], Ben J. Evans[2], and Kenneth Morgan[2]

[1]*BCAM—Basque Center for Applied Mathematics, Mazarredo, 14. 48009 Bilbao Basque Country, Spain*
[2]*College of Engineering, Swansea University, Singleton Park SA2 8PP, Swansea, Wales, UK*

(Received: 6 October 2014. Accepted: 29 October 2014)

ABSTRACT

This paper deals with fluidized sand simulation in order to estimate the impact of sand particle motion on the BLOODHOUND SuperSonic Car (SSC) drag forces, such phenomenon is known as a spray drag effect. A gas-particle model is used to simulate the sand particles that rise from the ground because of the strong shockwave-desert surface interaction. A finite volume scheme is used to discretise the continuous model with a special treatment of the solid phase equations. An indefinitely differentiable and anisotropic limiter to reinforce the method stability and reduce any excessive smearing is applied. To estimate the area where sand particles are detached from the ground, a criterion based on pressure change is proposed. The model is first validated on a curved 90° bend test case with comparison to experimental results and then applied to the supersonic car.

Keywords: Gas-Particle Mode, Drag Forces, Navier-Stokes Equations, Finite Volume Method, HLLC Solver.
Section: Mathematical, Physical & Engineering Sciences and Life

1. INTRODUCTION

The BLOODHOUND SSC (*Supersonic Car*) Project[(1)] was publicly announced in October 2008, with the objective of constructing a vehicle to take the World Land Speed Record to 1000 mph, see Figure 1 for an artist's impression of the car. To successfully achieve this feat, many major technological problems have been tackled. The aerodynamic design of the vehicle is one of them, and for this project it is exclusively based on computational fluid dynamic (CFD) simulations. This paper concentrates on one aspect, the study of the sand particle motion and impact with the vehicle on the drag forces (spray drag). As BLOODHOUND SSC travels at supersonic speed, the shockwaves created around the body of the car interact with the surroundings disturbing the desert surface. This causes sand and dust particles to rise up from the ground under the influence of pressure forces and these particles will then be moved up into the air by resistive drag forces. As the particles accelerate, their velocity overtake the velocity of the air resulting in a local air acceleration. Therefore, a critical amount of particles could significantly affect the flow and then create additional resistive forces acting on the car which are not typically accounted for in traditional CFD analysis. A Gas-Particle model (see for instance Refs. [2,3,6]) is proposed to simulate this phenomenon. In addition to the classical Navier-Stokes equations, a typical continuity equation of particle volume fraction is solved as well as a momentum equation where drag forces and gravity are considered for coupling. The numerical scheme is implemented within the FLITE package (see Refs. [4,5,11,33]). This package consists of a Delaunay mesh generator and a cell-centred finite volume flow solver. For the fluid phase, fluxes are estimated using a *Harten-Lax-van Leer-Contact* (HLLC) Riemann solver with a sigmoid-based limiter belonging to C^{∞}, the space of indefinitely differentiable functions (the derivatives of any order exist and are continuous),

*Author to whom correspondence should be addressed.
Email: lremaki@bcamath.org

Fig. 1. BLOODHOUND SSC artist's impression.

for better stability and convergence and with anisotropic action to reduce excessive smoothing. For the solid phase, a centred scheme is used. To stabilize the momentum equation we propose adding artificial viscosity with an orientation control coefficient that allow diffusion mostly in the streamline direction mimicking the *Streamline upwind Petrov-Galerkin* (SUPG) approach. The model is validated against experimental results from a 90° curved bend provided in Ref. [36]. Finally the model is applied to the BLOODHOUND SSC. To estimate the area where sand particles detach from the ground and entering the calculation domain, a criterion based on pressure change and gravity is proposed and applied to define the boundary condition on the ground for the particles volume fraction variable.

2. GOVERNING EQUATIONS

The equations governing three dimensional unsteady viscous compressible flow coupled with a particle motion equation in Eulerian modelisation can be expressed as:
Fluid phase:

$$\frac{\partial}{dt}(\phi_g\rho_g)+\nabla(\phi_g\rho_g U_g)=0, \quad \text{on } \Omega\times[o,T] \tag{1}$$

$$\frac{\partial}{dt}(\phi_g\rho_g U_g)+\nabla(\phi_g\rho_g U_g\otimes U_g) = -\nabla P_g+\nabla\tau_g-\beta(U_g-U_p), \quad \text{on } \Omega\times[o,T] \tag{2}$$

Particle phase:

$$\frac{\partial}{dt}(\phi_p\rho_p)+\nabla(\phi_p\rho_p U_p)=0, \quad \text{on } \Omega\times[o,T] \tag{3}$$

$$\frac{\partial}{dt}(\phi_p\rho_p U_p)+\nabla(\phi_p\rho_p U_p\otimes U_p) = -\frac{\phi_p}{\rho_p}\nabla P_g+\beta(U_g-U_p)+\phi_p\left(1-\frac{\rho_g}{\rho_p}\right)\vec{g}, \quad \text{on } \Omega\times[o,T] \tag{4}$$

where ϕ_g, ϕ_p are the gas and particle volume fractions satisfying the conservation condition with $\phi_g+\phi_p=1$,

$$\beta=\begin{cases}150\dfrac{\phi_p^2\mu_g}{\phi_g D_p^2}+1.75\dfrac{\phi_p\rho_g|U_p-U_g|}{D_p} & \text{if } \phi_g<0.8\\ \dfrac{3}{4}C_d\dfrac{\phi_p\rho_g|U_p-U_g|}{D_p}\phi_p^{-265} & \text{Else}\end{cases} \tag{5}$$

with

$$C_d=\begin{cases}\dfrac{24}{R_{e_p}}(1+0.15R_{e_p}^{0.687}) & \text{if } R_{e_p}<1000\\ 0.4 & \text{Else}\end{cases}$$

is the drag coefficient, $R_{e_p}=(D_p\phi_g|U_p-U_g|)/\nu_g$ is the particle Reynolds number, and $\vec{g}$ is the gravity.

In this model only drag and gravity forces are considered in the gas-particle interaction. Note that several drag formulas exist in the literature. We selected the one that gave satisfactory results according to examples in the literature (see for instance Ref. [6]).

3. NUMERICAL DISCRETISATION

A finite volume method described below is used to discretise the overall gas-particle model. In the solid phase, the particle volume fraction variable vanishes where the sand is absent which results in dividing by zero when computing the velocity vector in Eq. (4). This leads obviously to a severe instability of the scheme. To avoid this situation the non-conservative form of the momentum equation is considered, while the conservative form of the volume fraction is kept. The momentum equation takes the form:

$$\frac{\partial}{dt}(U_p)+\nabla(U_p\otimes U_p) = -\frac{1}{\rho_p}\nabla P_g+d_{fac}\frac{1}{\tau_p}(U_g-U_p)+\left(1-\frac{\rho_g}{\rho_p}\right), \quad \text{on } \Omega\times[o,T] \tag{6}$$

3.1. Finite Volume Method

For the sake of simplicity the finite volume method utilised for the Navier-Stokes equations without the solid phase coupling is described here. The Favre averaged equations governing three dimensional turbulent compressible flow are expressed, relative to a Cartesian (x_1, x_2, x_3) coordinate system, over a fixed volume V with a closed surface S, in the integral form

$$\frac{\partial}{\partial t}\int_V \vec{Q}\,dV=-\int_S \vec{F}^{\alpha}(\vec{Q})n^{\alpha}\,dS+\int_S \vec{G}^{\alpha}(\vec{Q})n^{\alpha}\,dS \quad \alpha=1,2,3 \tag{7}$$

where the summation convention is employed and $\vec{n}=(n^1,n^2,n^3)$ denotes the unit outward normal vector to S. In this equation, the unknown $\vec{Q}$, the inviscid flux vectors $\vec{F}^{\alpha}$ and the viscous flux vectors $\vec{G}^{\alpha}$ are defined by

$$\vec{Q}=\begin{pmatrix}\rho\\ \rho u_1\\ \rho u_2\\ \rho u_2\\ E\end{pmatrix} \quad \vec{F}^{\alpha}=\begin{pmatrix}\rho u_{\alpha}\\ \rho u_1u_{\alpha}+p\delta_{\alpha_1}\\ \rho u_2u_{\alpha}+p\delta_{\alpha_2}\\ \rho u_2u_{\alpha}+p\delta_{\alpha_3}\\ (E+p)u_{\alpha}\end{pmatrix}$$

$$\vec{G}^{\alpha} = \begin{pmatrix} 0 \\ \tau_{1\alpha} \\ \tau_{2\alpha} \\ \tau_{3\alpha} \\ u_{\beta}\tau_{\beta\alpha} - q_{\alpha} \end{pmatrix} \tag{8}$$

where ρ, p and E denote the averaged density, pressure and total energy of the fluid respectively, u_{α} is the averaged velocity of the fluid in direction x_{α}, t is the time and $\delta_{\alpha,\beta}$ is the Kronecker delta. The averaged deviatoric stress tensor is defined by

$$\tau_{\beta\alpha} = -\frac{2}{3}\mu\frac{\partial u_k}{\partial x_k}\delta_{\beta\alpha} + \mu\left(\frac{\partial u_{\beta}}{\partial x_{\alpha}} + \frac{\partial u_{\alpha}}{\partial x_{\beta}}\right) \tag{9}$$

and the averaged heat flux is given by

$$q_{\alpha} = -k\frac{\partial T}{\partial x_{\beta}} \tag{10}$$

In these equations, μ denotes the sum of the laminar and the turbulent viscosity, k is the sum of the laminar and the turbulent thermal conductivity and T is the averaged absolute temperature. The equation set is completed by the addition of the perfect gas equation of state. The laminar viscosity is assumed to vary with temperature according to the Sutherland Law[7] and the distribution of the turbulent viscosity is determined using a one equation Spalart–Allmaras model.[8] The Prandtl number is taken to be constant. Steady state solutions of the resulting equation set are sought in a fixed spatial computational domain Ω.

On the generated consistent hybrid primal mesh, nodes are located at the vertices of the elements and the spatial discretisation of Eq. (1) is accomplished using a cell vertex finite volume method. This requires the construction of a dual mesh, in which each cell of the dual is associated with a single node of the primal mesh. For those regions in which the primal mesh consists only of isotropic tetrahedral cells, a median dual mesh is constructed by connecting cell edge midpoints, cell centroids and cell face centroids, such that only one node is present within each dual mesh cell.[9] With this strategy, each node I of the domain mesh is associated with a volume Ω_I of the dual mesh. The boundary surface of the volume Ω_I is denoted by Γ_I. Each edge of the domain mesh is associated with a segment of the dual mesh interface between the nodes connected to the edge. This segment is a surface constructed from triangular facets, where each facet is connected to the midpoint of the edge, a neighboring element centroid and the centroid of an element face connected to the edge, as illustrated in Figure 2(a). The midpoint of the edge between node I and J is denoted by $\vec{x}_m^{IJ}$, the centroid of the face with vertices I, J and K is denoted by $\vec{x}_s^{IJK}$ and the element centroid is designated by $\vec{x}_c$. The bold lines on the dual mesh in this figure illustrate the boundaries

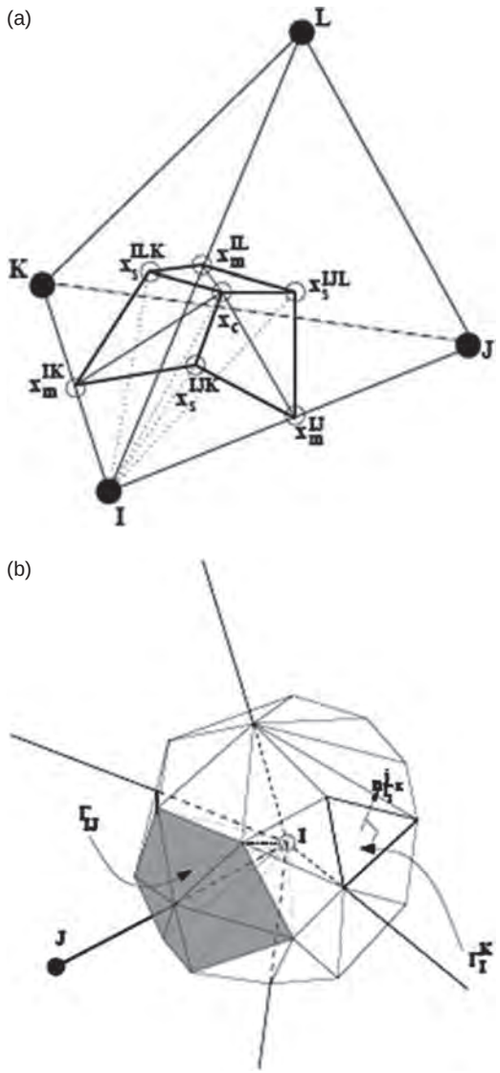

Fig. 2. (a) Illustration of that part of the dual mesh cell surrounding node I that is contained within a tetrahedral cell. (b) Illustration of the dual mesh cell surrounding an internal node I.

between the edges with which the dual mesh segment is associated. With this dual mesh definition, the volume Ω_I can be viewed as being constructed in terms of a set of tetrahedra, as illustrated for a typical interior node I in Figure 2(b). The surface of the dual mesh cell surrounding node I is defined in terms of the closed set of planar triangular facets Γ_I^K, where each facet only touches a single edge of the domain mesh. The set of facets touching the edge between nodes I and J is denoted by Γ_{IJ}.

In general, the median dual approach cannot be used for the hybrid elements produced by merging the stretched tetrahedra generated by the advancing layers method. This is because cells created in this way may be warped so severely that a vertex can lie outside the corresponding median dual cell. This may occur in regions of high geometry curvature or at the interface between the hybrid and

isotropic meshes. To overcome this problem, the information contained in the primal tetrahedral mesh is used to ensure that the topology of the control volume cells is valid.[9]

Equation (1) is applied to each cell Ω_I of the dual mesh in turn. To perform the numerical integration of the inviscid fluxes over the surface Γ_I of this cell, a set of coefficients is calculated for each edge using the dual mesh segment associated with the edge. The values of these coefficients for an internal edge are evaluated as[37,38]

$$n_{IJ}^{\alpha} = \sum_{K \in \Gamma_{IJ}} A_{\Gamma_I^K} n_{\Gamma_I^K}^{\alpha} \tag{11}$$

where $A_{\Gamma_I^K}$ is the area of facet Γ_I^K and $n_{\Gamma_I^K}^{\alpha}$ is the component, in direction x_α, of the outward unit normal vector of the facet from the viewpoint of node I. The integral of the inviscid flux over the surface Γ_I is then approximated, using the summation of edge contributions, as[37,39]

$$\int_{\Gamma_I} \vec{F}^{\alpha} n^{\alpha} dS \approx \sum_{J \in \Lambda_I} \tilde{\vec{F}}_{IJ} \tag{12}$$

where Λ_I denotes the set of nodes connected to node I by an edge in the domain mesh. Here,

$$\tilde{\vec{F}}_{IJ} = \begin{pmatrix} \rho q_{IJ} \\ \rho u_1 q_{IJ} + p n_{IJ}^1 \\ \rho u_2 q_{IJ} + p n_{IJ}^2 \\ \rho u_3 q_{IJ} + p n_{IJ}^3 \\ (E+p) q_{IJ} \end{pmatrix} \tag{13}$$

is a consistent numerical inviscid flux function and

$$q_{IJ} = n_{IJ}^{\alpha} (u_{\alpha})_I \tag{14}$$

is the velocity in the direction of the edge connecting nodes I and J. Similarly, the integral of the viscous flux over the surface Γ_I is approximated as

$$\int_{\Gamma_I} \vec{G}^{\alpha} n^{\alpha} dS \approx \sum_{J \in \Lambda_I} \vec{G}_{IJ} = \sum_{J \in \Lambda_I} \frac{n_{IJ}^{\alpha}}{2} (\vec{G}_I^{\alpha} + \vec{G}_J^{\alpha}) \tag{15}$$

where the physical viscous flux function is employed.[?] The solution is advanced in time to steady state using an explicit multi-stage Runge Kutta procedure and the convergence is accelerated by the use of local time stepping and by the addition of an agglomerated multigrid process.

3.2. Inviscid Fluxes Estimation

3.2.1. Fluid Phase

The inviscid fluxes of the fluid phase are estimated using a second order HLLC *Riemann* solver and the limiter developed in Ref. [10]. In the following, the limiter formulation is briefly described. To obtain a second order HLLC solver, the quantities Q_{IJ}^L and Q_{IJ}^R of a typical primitive scalar variable Q, employed in the HLLC formulation of the *Riemann* problem, are replaced by the expressions

$$\tilde{Q}_{IJ}^L = Q_{IJ}^L + \vec{h}_{IJ} \cdot \nabla Q_I \quad \tilde{Q}_{IJ}^R = Q_{IJ}^R + \vec{h}_{JI} \cdot \nabla Q_J \tag{16}$$

where $\vec{h}_{IJ} \cdot \nabla Q_I$ and $\vec{h}_{JI} \cdot \nabla Q_J$ denote appropriate gradient approximations. To ensure stability for simulations of flows involving discontinuities or steep gradients, the reconstructed gradient must be limited in some fashion. To avoid oscillatory scheme, first we force the local extremum diminishing (LED) property to be satisfied which guaranties that we always have

$$\min_{J \in \Lambda_I} (Q_J - Q_J) \le \vec{h}_{IK} \cdot \nabla Q_I \le \max_{J \in \Lambda_I} (Q_J - Q_J) \tag{17}$$

This is achieved using the following limiter

$$\Phi_{IK} = \begin{cases} sg_n\left(\dfrac{\max_{J \in \Lambda_I}(Q_J - Q_I)}{\vec{h}_{IK} \cdot (\nabla Q)_I}\right) & \text{if } \vec{h}_{IK} \cdot \nabla Q_I > 0 \\ sg_n\left(\dfrac{\min_{J \in \Lambda_I}(Q_J - Q_I)}{\vec{h}_{IK} \cdot \nabla Q_I}\right) & \text{if } \vec{h}_{IK} \cdot \nabla Q_I < 0 \\ 1 & \text{otherwise} \end{cases} \tag{18}$$

where $sg_n(t) = t/(1+t^n)^{1/n}$.

The reconstructed gradient $\vec{h}_{IK} \cdot \nabla Q_I$ is then replaced by $\Phi_{IK} \vec{h}_{IK} \cdot \nabla Q_I$. Such a limiter has many advantages; it is indefinitely differentiable which improves the overall scheme convergence. It provides a gradual gradient normalization that maintains the local variation behavior of the solution. In addition the $sg_n(t)$ function has the attractive property $sg_n(t) \le t$ and $sg_n(t) \le 1$ for $t \ge 0$ that guaranties the condition (17) to be always satisfied with the non-amplification of local gradients. Furthermore, $sg_n(t)$ is a good approximation of the minimum function, since

$$\lim_{n \to \infty} (sg_n(t)) = \min(1, t) \quad \text{for } t \ge 0 \tag{19}$$

For the tests of this paper, the value $n = 2$ is used.

Note that we don't take the minimum of Φ_{IK} as it is usually the case, which leads to an anisotropic limiting. The advantage of doing so is that the likely excessive limiting (due to taking the minimum) that results in excessive diffusion is reduced. However the conservation property is violated. To remedy this situation we proceed as in Ref. [11] by imposing the following conservation condition

$$\Phi_{IJ} \vec{h}_{IJ} \cdot \nabla Q_I = -(\Phi_{JI} \vec{h}_{JI} \cdot \nabla Q_J) \tag{20}$$

This condition could be satisfied by using a *minmod* function where $\Phi_{IJ} \vec{h}_{IJ} \cdot \nabla Q_I$ and $\Phi_{JI} \vec{h}_{JI} \cdot \nabla Q_J$ are replace by $\text{minmod}(\Phi_{IJ} \vec{h}_{IJ} \cdot \nabla Q_I, \Phi_{JI} \vec{h}_{IJ} \cdot \nabla Q_J)$ and $-\text{minmod}(\Phi_{IJ} \vec{h}_{IJ} \cdot \nabla Q_I, \Phi_{JI} \vec{h}_{IJ} \cdot \nabla Q_J)$ respectively. The minmod function is defined as

$$\text{minmod}(a, b) = \begin{cases} 0 & \text{if } ab < 0 \\ \text{else} & \\ a & \text{if } |a| \le |b| \\ b & \text{if } |a| \ge |b| \end{cases} \tag{21}$$

3.2.2. Particle Phase

A centered scheme is used for the non-conservative momentum equations of the particle phase, and it is stabilized by adding a first order artificial viscosity of the form

$$\triangle Q_i = \sum_{J \in N_I} \lambda_{IJ}(Q_J - Q_I) \tag{22}$$

To allow diffusion to act mostly in the flow direction while minimizing the cross wind effects similar to streamline diffusion methods, we propose the coefficients λ_{IJ} to have the following form:

$$\lambda_{IJ} = \frac{1}{1 + \tan(\theta_{IJ})^2} \tag{23}$$

Where θ_{IJ} is the angle between the normal to the surface η_I and the velocity vector U_I.

For the conservative continuity equation, recall that to estimate the flux at each interface, a typical equation $(\partial/dt)(\phi_p) + q_{IJ}(\partial/ds)(\phi_p) = 0$ is considered, where $q_{IJ} = U_p^I \eta_{IJ}$, U_P^I being the particle velocity at node I and η_{IJ} the normal to the surface separating dual cells associated with node I and J. This equation is solved using a Riemann solver.

4. VALIDATION

Before applying the gas-particle model described above to the assessment of fluidized sand impact on drag forces, the model is validated against experimental results of a 90° bend test case described in Ref. [36]. This test case was selected first because of the availability of experimental data and then for the wide use of curved ducts in industrial applications such as air-coal flows in coal combustion equipment, coal liquefaction-gasification pipe systems, gas-particle flows in turbo machinery, and contaminant particle flows in ventilation ducts. The apparatus and geometry of the test are shown in Figure 3 scanned from the Ref. [36]. The 90° duct has a square cross-section of $D = 0.1$ m and upstream and downstream duct lengths are 1 m and 1.2 m, respectively. Glass spherical particles with a material density of 2990 kg/m^3 and diameter size of 50 m are used. The inlet fluid and particle velocity is set to 52.19 m/s, for more details see Ref. [36]. For the numerical simulation a hybrid mesh is used as shown in Figure 4. The mesh contains 766614 tetrachordal elements and 1229952 prisms forming 12 boundary layers. The computational domain starts $10D$ upstream from the bend entrance and extends up to $12D$ downstream from the bend exit. The classical viscous flow boundary conditions are imposed for the fluid phase, typically pressure inlet, pressure outlet, and non-slip wall condition. For the initial condition we considered a uniform zero velocity and constant temperature of 273.15 Kelvin, and a constant density of 1.2886 kg/m^3. A rebounding particle-wall conditions with normal and tangential restitution coefficients of 0.9 and 0.8 respectively, are considered for the solid phase. Finally, the turbulence features are captured using the *Shear Stress Transport* (SST) turbulence model. The simulation ran on 20 cores of a PC Cluster based on quad core AMD Opteron 240 1.4 Ghz processors and 4 Gig of memory per processor. The PC Cluster makes use of a 2 Gbit/s Myrinet Optical Fibre interconnect and parallelisation was implemented using MPI. The simulation required 24 hours wall-clock time for convergence.

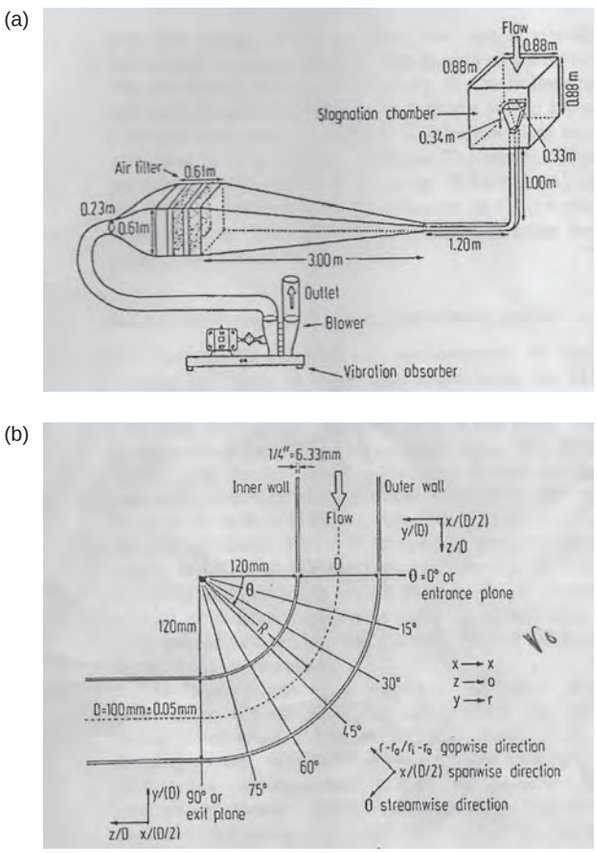

Fig. 3. Experimental apparatus: (a) General flow system, (b) geometry of the curved square duct.

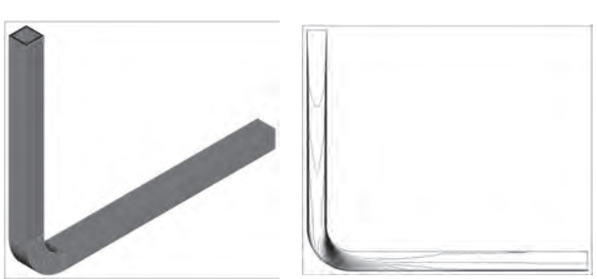

Fig. 4. Hybrid used mesh and volume fraction profile for the curved duct.

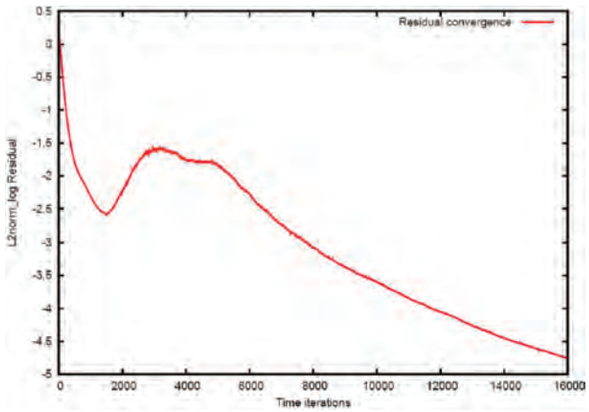

Fig. 5. Bend case: Residual convergence.

4.1. Results

Figure 4 shows the used mesh and the particles volume fraction profile. Figure 5 show the residual convergence that drops by 5 orders of magnitude. Figure 6 shows a good agreement of the fluid and particles mean stream velocity with experimental results for the different stations shown in 3(b), that are lines perpendicular to the bend wall and belonging to the cutting plan that contains the central dash line of the figure. This demonstrates the validity and the accuracy of the physical and numerical models, which motivates and justifies its application to the BLOODHOUND SSC.

5. APPLICATION TO BLOODHOUND SSC

After validating the gas-particle model and the numerical scheme described above, the model is applied to simulate sand particles entrained by the flow around the BLOODHOUND SSC which is the targeted application in this work. The imposed running conditions are Mach number, $M = 1.3$, angle of attack, AoA $= 0.0$ and Reynolds number, Re $= 13752000$. For the initial condition we considered a uniform velocity of 445.9 m/s and constant temperature of 273.15 Kelvin, and a constant density of 1.2886 kg/m^3. The sand characteristics are $D = 0.08$ mm and $\rho_p = 1850$ kg/m^3. A hybrid mesh is generated using FLITE package (described Refs. [4 and 5]).

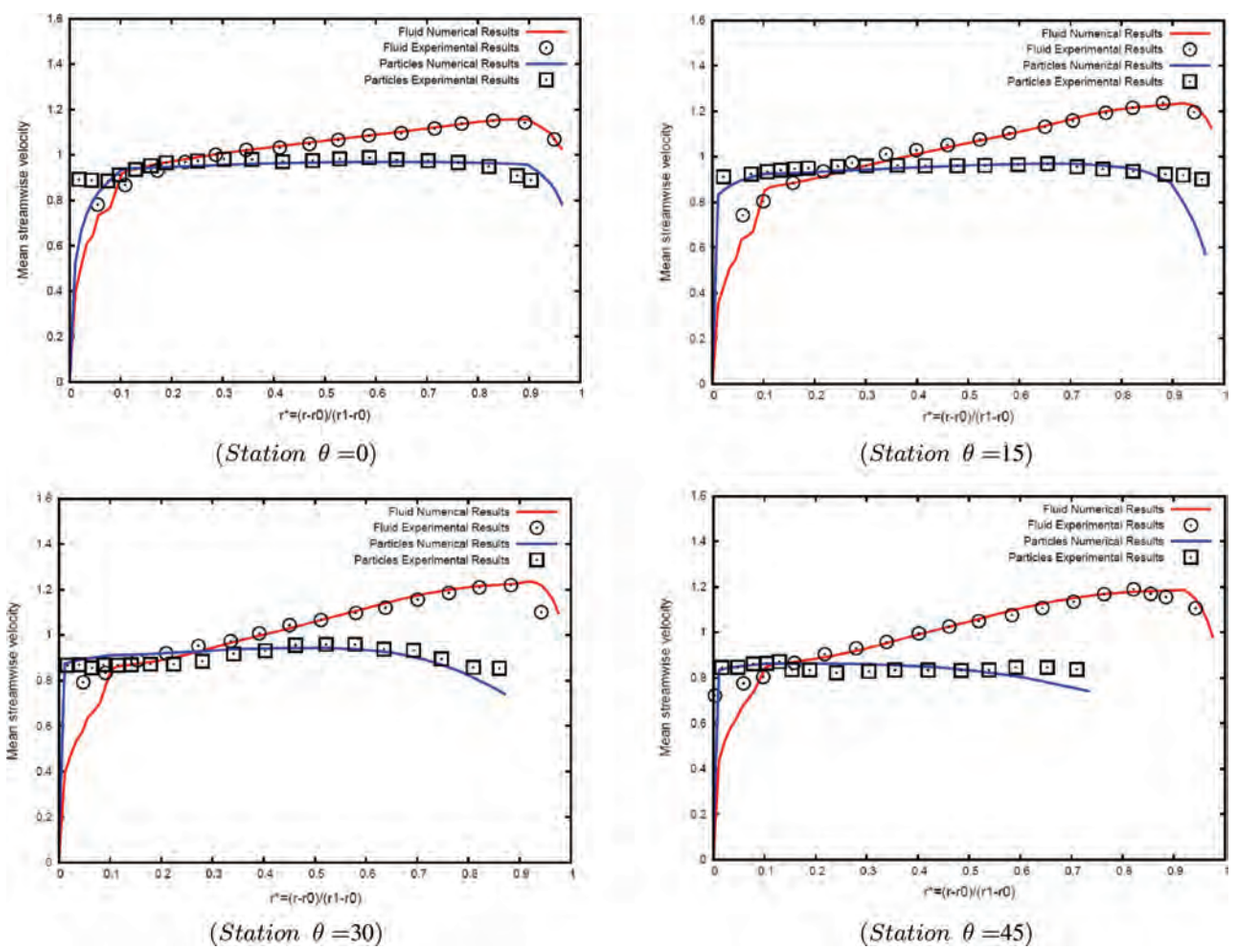

Fig. 6. 90° Bend case: Mean stream fluid and particles velocity comparison to experimental results for the different stations.

5.1. Boundary Conditions

The far-field boundary condition is imposed for the fluid phase and the slip condition is considered on the wall (ground) to simulate ground motion. A tangential velocity is imposed to the wheels to simulate rotation since they are considered as full discs. The particle volume fraction boundary conditions on the ground are not obvious however. The amount of particles (sand) that should be injected into the air and the area where they should be released is not clear. In our case the variation of the pressure is considered as the principle cause of sand rising, therefore the gradient of pressure in the normal direction normalized by the gravity is selected as a criterion to define the sand entrainment area (see Eq. (24)). More precisely particles are injected in the air if $\vartheta > 1$. This means that particles are released if the pressure decreases just above the ground in one hand and the exerted pressure force is greater than the one exerted by the gravity. Note that we neglected the friction. As for the quantity of sand to inject, a uniform concentration is imposed and different values of volume fraction, namely 1.5×10^{-3}, 5×10^{-3} and 5×10^{-2} are selected. This choice is based on the maximum fraction volume values recorded on the near center of a sandstorm (this information could be obtained by UK weather for example), which are of the order 10^{-3}. This choice is motivated by the fact that the car speed can't rise up more particles than violent sandstorms, and this value is considered as the worst case limit.

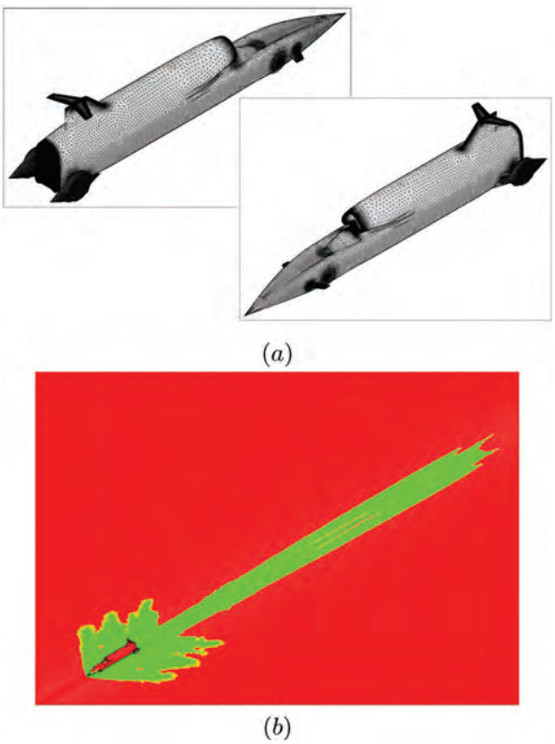

Fig. 7. (a) BLOODHOUND SSC: Hybrid mesh, (b) the delimited area using ϑ criterion.

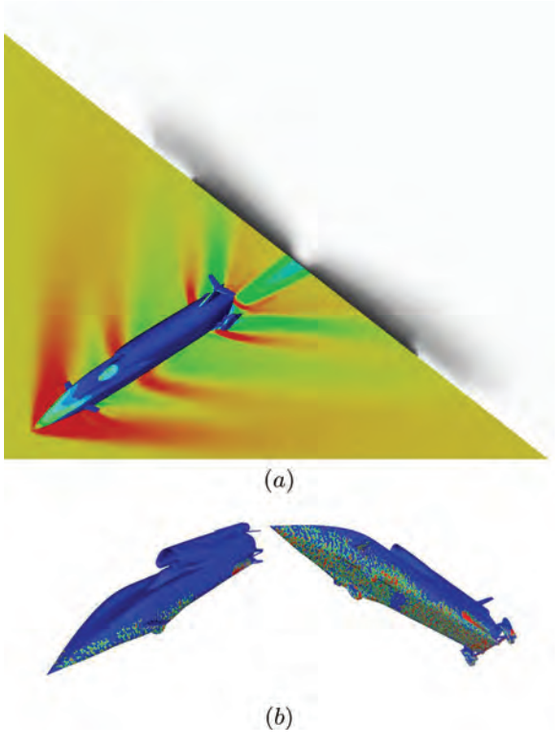

Fig. 8. (a) Volume fraction cuts plan, (b) sand distribution on car underside.

$$\vartheta = \frac{-(1/\rho_p)\nabla P \vec{\eta}}{g} \tag{24}$$

where $\vec{\eta}$ is the normal to the ground and g is the gravity.

5.2. Results

Figure 7 shows the used mesh and the delimited area obtained using the pressure criterion. The mesh contains 12384068 tetrahedral elements with 12 prismatic layers in

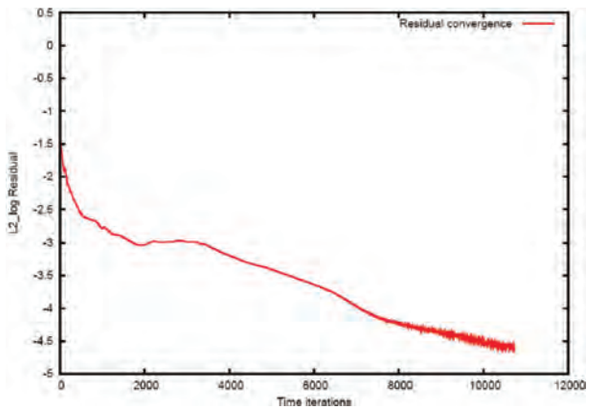

Fig. 9. Residual convergence.

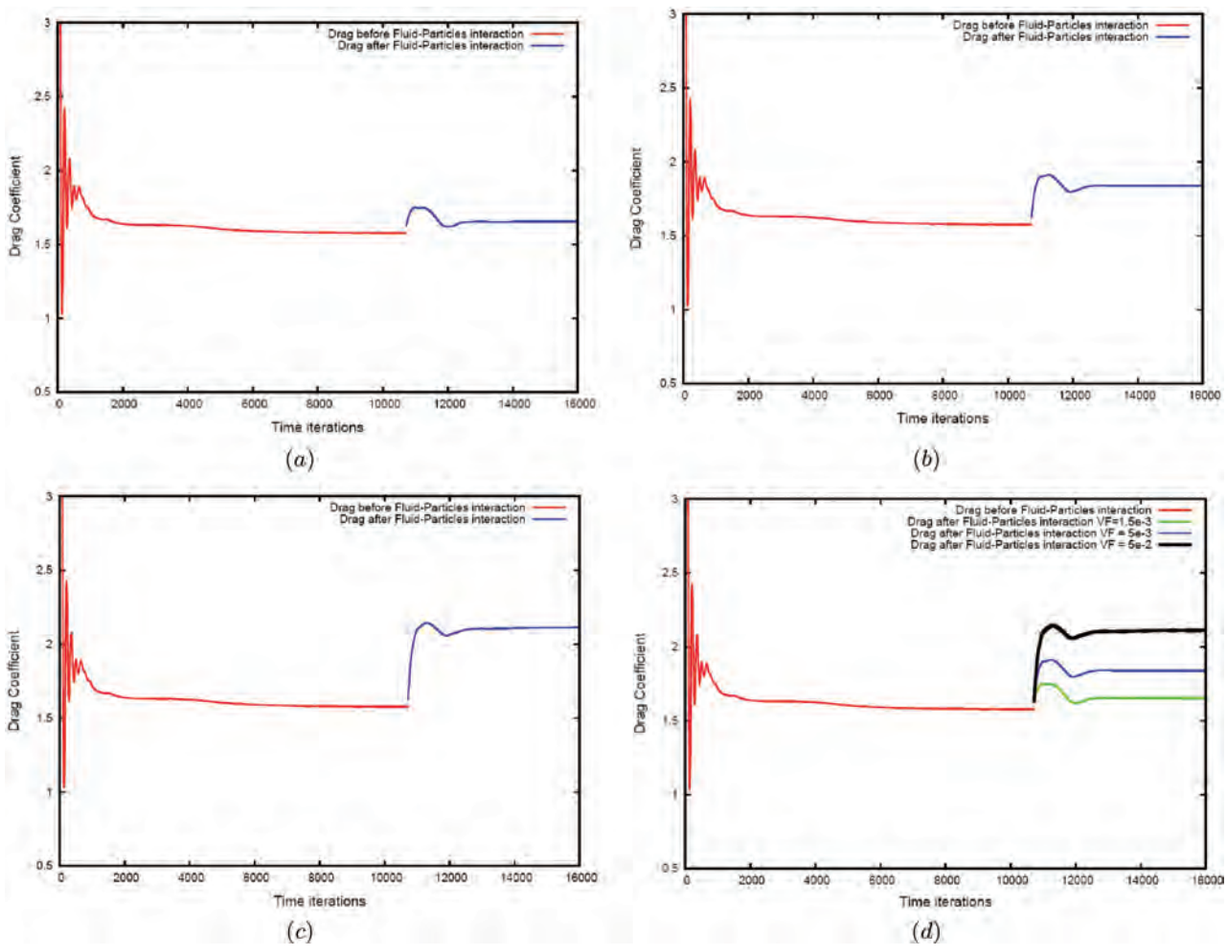

Fig. 10. Drag convergence before and after injecting sand particles: (a) Volume fraction $= 1.5 \times e^{-3}$, drag increases by 5%. (b) Volume fraction $= 5 \times e^{-3}$, drag increases by 10%. (c) Volume fraction $= 5 \times e^{-2}$, drag increases by 20%. (d) Comparison of drag jump with volume fraction.

the boundary layer mesh. A cut plan in Figure 8 shows the propagation of a sand particle cloud behind the car and fluid density is plotted on the ground and particles velocity profile on the car. Particles of sand on the underneath of the car are shown also. Figure 9 shows the residual convergence that drops by 4 orders of magnitude. Figure 10 show the drag convergence before and after sand particles injection. To the different values of volume fraction injected from the ground 1.510^{-3}, 510^{-3} and 510^{-2}, correspond a drag increase of 5%, 10% and 20% respectively. Using the maximum fraction volume values near the centre of a sandstorm (of the order 10^{-3} as mentioned above) the expected increase of drag due to the spay drag phenomenon, will not exceed 10%. This increase, from the aerodynamic point of view, is acceptable and don't require any aerodynamic shape change of the Bloodhound SCC. Note that the simulation using the same cluster described before, run on 128 cores and took 35 hours wall-clock time for convergence.

6. CONCLUSIONS

The paper presented a spray drag analysis using a gas-particle model to predict the impact of sand particles entrained from the ground into an aerodynamic flow because of shockwave-ground interaction on the BLOODHOUND SuperSonic Car. The model is dicretized using a dual mesh finite volume scheme. The HLLC solver is used to estimate inviscid fluxes for the fluid with a sigmoid-based limiter that has the nice property to indefinitely differential. The limiter acts in anisotropic way to avoid excessive limiting and then a conservative condition is added using *minmod* function. A centred scheme is used for the momentum equation stabilized by adding artificial viscosity with orientation control coefficient that allow diffusion mostly in the streamline direction mimicking the SUPG technique. A validation of the physical and numerical models is achieved on a 90 curved bend. The model is then applied to BLOODHOUND SSC to predict the effect of sand particle entrainment on drag forces. Specific boundary condition of the volume fraction variable

is used to estimate the area where the particles penetrate the calculation domain, then a uniform concentration is imposed based on a reference values from registered sandstorms. The results show a drag increase of no greater than 10% Which is considered acceptable and don't require any aerodynamic adjustment of the car.

References and Notes

1. B. J. Evans, J. W. Jones, K. Morgan, O. Hassan, and L. Remaki; Computational fluid dynamics applied to the aerodynamic design of a land-bases supersonic vehicle; *Journal of Partial Differential Equation* 27, 141 **(2011)**.
2. Y. Liu, F. Jiang, X. Li, and G. Li; Effect of drag force on backward-facing step gas-particle turbulent flows; *Heat Mass Transfer* 50, 803 **(2014)**.
3. A. Passalacqua and R. O. Fox; Advanced continuum modelling of gas-particle flows beyond the hydrodynamic limit; *Applied Mathematical Modelling* 35, 1616 **(2011)**.
4. K. A. Sørensen, O. Hassan, K. Morgan, and N. P. Weatherill; A multigrid accelerated time-accurate inviscid compressible fluid flow solution algorithm employing mesh movement and local remeshing; *Int. J. Num. Meth. Fluids* 45, 517 **(2003)**.
5. N. P. Weatherill, O. Hassan, K. Morgan, J. W. Jones, B. G. Larwood, and K. A. Sørensen; Aerospace simulations on parallel computers using unstructured grids; *Int. J. Num. Meth. Fluids* 40, 171 **(2002)**.
6. A. Samuelsberg and H. B. Hjertager; Computational modeling of gas/particle flow in a riser; *AIChE J.* 42, 1536 **(2004)**.
7. F. M. White; Viscous Fluid Flow, 3rd edn., McGraw Hill, Boston **(2006)**.
8. P. R. Spalart and S. R. Allmaras; A one-equation turbulent model for aerodynamic flows; AIAA Paper 92-0439 **(1992)**.
9. K. A. Sørensen; A Multigrid Accelerated Procedure for the Solution of Compressible Fluid Flows on Unstructured Hybrid Meshes; Ph.D. Thesis, University of Wales, Swansea **(2002)**.
10. L. Remaki, O. Hassan, and K. Kenneth; New limiter and gradient reconstruction method for hllc-finite volume scheme to solve Navier-Stokes equations, *TECCOMAS, the fifth European Congress on Computational in Fluid Dynamic*, Lisbon, Portugal, June **(2010)**.
11. L. Remaki, O. Hassan, and K. Kenneth; A high order finite volume-HLLC solver and anisotropic delaunay mesh adaptation; *The 47th AIAA Aerospace Sciences Meeting and Exhibit*, Orlando, Florida, USA, January **(2009)**, AIAA-2009-1498.
12. L. Remaki and M. Cheriet; Numerical scheme of shock filter models for image enhancement and restoration; *Journal of Mathematical Imaging and Vision* 18, 129 **(2003)**.
13. L. Remaki; Theoretical and Numerical Study of Quasi-Linear Equations with Discontinuous Coefficients, and 2D Linear Acoustic; Ph.D. Thesis, Claude Bernard University, France **(1997)**.
14. L. Remaki, O. Hassan, and K. Kenneth; Aerodynamic computations using a finite volume method with an HLLC numerical flux function; *J. Mathematical Modeling of Natural Phenomena* 6, 189 **(2011)**.
15. O. C. Zienkiewicz and R. C. Taylor; The Finite Element Method; 4th. edn., McGraw Hill, New York **(1989)**, Vol. I **(1991)**, Vol. II.
16. S. Idelsohn and E. Oñate; Finite element and finite volumes, Two good friends; *Int. J. Num. Meth. Engng.* 37, 3323 **(1994)**.
17. R. Abgrall, M. Ricchiuto, N. Villedieu, C. Tavé and H. Deconinck; Very high order residual distribution on triangular grids; *Proceedings of the European Conference on Computational Fluid Dynamics, ECCOMAS CFD 2006*, edited by P. Wesseling, E. Oñate, and J. Periaux, Egmond aan Zee, Netherlands **(2006)**, Paper no 583.
18. V. Girault and P.-A. Raviart; Finite Element Methods for the Navier Stokes Equations, Springer, Berlin **(1986)**.
19. A. Corsini; A FE Method for the Computational Fluid Dynamics of Turbomachinery, Lecture Notes **(1999)**.
20. R. Eymard, T. Galluöet, and R. Herbin; Finite volume methods, Handbook of Numerical Analysis; North Holland, Amsterdam **(2000)**, Vol. 7, pp. 713–1020.
21. C. Chainais-Hillairet; Finite volume schemes for a nonlinear hyperbolic equation: Convergence towards the entropy solution and error estimates; *M2AN Math. Model. Numer. Anal.* 33, 129 **(1999)**.
22. P.-H. Cournède, C. Debiez, and A. Dervieux; A positive MUSCL scheme for triangulations; Research Report INRIA, RR-3465 **(1998)**.
23. J. A. Desideri and A. Dervieux; Compressible flow solvers using unstructured grids, Von Karman Institute Lecture Notes 1988–05, Von Karman Institute for Fluid Dynamics, Belgium **(1988)**.
24. R. E. Ewing, T. Lin, and Y. Lin; On the accuracy of the finite volume element method based on piecwise linear polynomials; *SIAM J. Numer. Anal.* 39, 1865 **(2002)**.
25. E. F. Toro, M. Spruce, and W. Speares; Restoration of the contact surface in the HLL–Riemann Solver; *Shock Waves* 4, 25 **(1994)**.
26. E. F. Toro; Riemann Solvers and Numerical Methods for Fluid Dynamics, A Practical Introduction, 2nd edn., Springer, Berlin **(1999)**.
27. S. Taasan and D. M. Nark; An absorbing buffer zone technique for acoustic wave propagation; AIAA Paper 95-0164 **(1995)**.
28. J. Peraire, J. Perió, and K. Morgan; Adaptive remeshing for three-dimensional compressible flow computation; *J. Comp. Phys.* 103, 269 **(1992)**.
29. W. G. Habashi, J. Dompierre, Y. Bourgault, D. Ait-Ali-Yahia, M. Fortin, and M.-G. Vallet; Anisotropic mesh adaptation: Towards user-independent, mesh-independent and solver-independent CFD solutions. Part I: general principles; *Int. J. Num. Meth. Fluids* 32, 725 **(2000)**.
30. E. F. D'Azevedo and R. B. Simpson; On optimal triangular meshes for minimizing the gradient error; *Núm. Math.* 59, 321 **(1991)**.
31. M. Fortin; Anisotropic mesh adaptation through hierarchical error estimators; *SIAM J. Numer. Anal.* 26, 788 **(1998)**.
32. V. Dolejsi and J. Felcman; Anisotropic mesh adaptation for transonic and supersonic flow simulation; *Proceedings of Algoritmy Conference on Scientific Computing* **(2002)**, pp. 78–85.
33. L. Remaki and W. G. Habashi; 3-D mesh adaptation on multiple weak discontinuities and boundary layers; *SIAM J. Sci. Comput.* 28, 1379 **(2006)**.
34. L. Remaki, C. Lepage, and W. G. Habashi; Efficient anisotropic mesh adaptation on weak and multiple shocks; AIAA Paper 2004-0084 **(2004)**.
35. D. J. Mavriplis; Revisiting the least-squares procedure for gradient reconstruction on unstructured meshes; AIAA Paper 2003-3986 **(2003)**.
36. Y. Kliafas and M. Holt; LDV measurements of a turbulent airsolid twophase flow in a 90° bend; *Experiments in Fluids* 5, 73 **(1987)**.
37. K. Morgan and J. Peraire; Unstructured grid finite element methods for fluid mechanics; *Rep. Prog. Phys.* 61, 569 **(1998)**.
38. P. R. M. Lyra; Unstructured grid adaptive algorithms for fluid dynamics and heat conduction, Ph.D. Thesis, University of Wales, Swansea **(1994)**.
39. J. Peraire, J. Peiró, and K. Morgan; Finite element multigrid solution of Euler flows past installed aero-engines; *Comp. Mech.* 11, 433 **(1993)**.